Nanoscale

Scalable two-tier protruding micro-/nano-optoelectrode arrays with hybrid optical-electrical modalities by hierarchical modular design

Journal:	*Nanoscale*
Manuscript ID	NR-ART-07-2022-003820.R1
Article Type:	Paper
Date Submitted by the Author:	25-Sep-2022
Complete List of Authors:	Mejia, Elieser; Virginia Tech Song, Junyeob; NIST Zhao, Yuming; Virginia Tech, Electrical and Computer Engineering Qian, Yizhou; Virginia Tech Xiao, Chuan; Virginia Tech, Electrical and Computer Engineering; Virginia Tech Lezec, Henri; NIST Agrawal, Amit; NIST Zhou, Wei; Virginia Tech, Electrical and Computer Engineering; Virginia Tech

Scalable two-tier protruding micro-/nano-optoelectrode arrays with hybrid optical-electrical modalities by hierarchical modular design

Elieser Mejia, Junyeob Song, Yuming Zhao, Yizhou Qian, Chuan Xiao, Henri J. Lezec, Amit Agrawal, and Wei Zhou*

Elieser Mejia, Yuming Zhao, Yizhou Qian, Chuan Xiao, Dr. Wei Zhou

Department of Electrical and Computer Engineering, Virginia Tech, Blacksburg, VA 24061, USA

E-mail: wzh@vt.edu

Dr. Junyeob Song

Department of Electrical and Computer Engineering, University of Delaware, Newark, DE 19716, USA

Dr. Junyeob Song, Dr. Henri J. Lezec, Dr. Amit Agrawal

National Institute of Standards and Technology, Gaithersburg, MD 20899, USA

Keywords: multiresonant plasmonic nanoantenna, multi-electrode array, micropillar

Abstract: *In situ* spatiotemporal characterization of correlated bioelectrical and biochemical processes in living multicellular systems remains a formidable challenge but can offer crucial opportunities in biology and medicine. A promising approach is to develop bio-interfaced multifunctional micro-/nano-sensor arrays with complementary biophotonic-bioelectronic modalities and biomimetic topology to achieve combined bioelectrical and biochemical detection and tight device-cell coupling. However, a system-level engineering strategy is still missing to create multifunctional micro-/nano-sensor arrays that meet the multifaceted design requirements for *in situ* spatiotemporal characterizations of living systems. Here, we demonstrate a hierarchical modular design and fabrication approach to develop scalable two-tier protruding micro-/nano-optoelectrode arrays that extend the design space of biomimetic micro-/nano-pillar topology, plasmonic nanoantenna-based biophotonic function in surface-enhanced Raman spectroscopy (SERS), and micro-/nano-electrode-based bioelectronics function in electrochemical impedance spectroscopy (EIS). Notably, two-tier protruding micro-/nano-optoelectrode arrays composed of nanolaminate nanoantenna arrays on top of micropillar electrode arrays can support plasmonic nanocavity modes with high SERS enhancement factors ($\approx 10^6$) and large surface-to-volume ratio with significantly reduced interfacial impedance in EIS measurements. We envision that scalable two-tier protruding micro-/nano-optoelectrode arrays can potentially serve as bio-interfaced multifunctional micro-/nano-sensor arrays for *in situ* correlated spatiotemporal bioelectrical-biochemical measurements of living multicellular systems such as neuronal network cultures, cancerous organoids, and microbial biofilms.

1. Introduction

Living multicellular systems, ranging from neuronal networks to cancerous tumors and microbial biofilms, feature dynamic, heterogeneous, and adaptive biological activities coordinated by cellular interactions through various bioelectrical and biochemical signaling

pathways.[1] Unfortunately, conventional bioanalysis methods based on single-modal end-point measurements have difficulty resolving spatiotemporal correlations between bioelectrical and biochemical processes in living systems, impeding the understanding of complex biological activities from a holistic systems-biology approach. Therefore, it is desirable to establish new methods for multimodal spatiotemporal measurements of multiple correlated bioelectrical and biochemical processes across multicellular systems.[2] A potential approach is to develop bio-interfaced multifunctional micro-/nano-sensor arrays with complementary bioelectronic-biophotonic detection modalities to allow multimodal spatiotemporal measurements of living multicellular systems.

With the increasing availability of micro-/nano-fabrication tools, the past two decades have seen significant advances in micro-/nano-scale bioelectronic and biophotonic devices for biosensing and bioanalysis of living systems.[3-19] For example, micro-/nano-electrode arrays have demonstrated great utility for spatiotemporal measurements of bioelectrical activities in networks of electrogenic cells, including neurons and cardiac myocytes.[11-15] Notably, micro-/nano-electrodes with protruding biomimetic topologies, such as micro-/nanopillar structures, can elicit spontaneous cell engulfment behaviors for a tight device-cell coupling to achieve intracellular-like electrical recording of membrane potentials in electrogenic cells.[16, 17] On the other hand, plasmonic nanoantennas made of noble metal nanostructures can concentrate light at the nanoscale to enable surface-enhanced Raman spectroscopy (SERS) biochemical analyses of living cells with molecular vibrational fingerprint information.[18, 19] Despite the apparent benefits, there is little research in developing micro-/nano-optoelectrodes (*i.e.*, combined micro-/nano-electrode and nanoantenna devices) in large arrays for multimodal spatiotemporal measurements of bioelectrical and biochemical information in living systems. In particular, there is a lack of a system-level modular design approach to create bio-interfaced micro-/nano-optoelectrode arrays with optimized hybrid device properties for achieving multimodal

bioelectrical recording, SERS biochemical analyses, and tight nanodevice-cell coupling by biomimetic design. A significant challenge limiting the modular design space resides in the difficulty of patterning nanoscale features on non-planar large-scale (cm scale) areas using conventional nanofabrication techniques such as electron-beam lithography or ion-beam milling. Alternatively, light can be used to pattern both micro- and nanoscale features, opening opportunities for a modular design approach. For example, modern additive fabrication techniques based on stereolithography[20] and 2-photon polymerization[21] have enabled rapid prototyping of complex 3D micro-/nano-scale features, which potentially can be used to create next-generation micro-/nanostructured optical, electrical, and mechanical systems. Standard mask/maskless photolithography-based fabrication techniques have also been employed to create 3D micro-scale features with sizes constrained by the diffraction limit and penetration depth of UV light in photoresists. Advanced photolithography techniques using phase-shifting interference effects can directly generate nano-patterns.[22, 23] Despite significant efforts, it remains challenging for existing light-based fabrication techniques to achieve modularized integration of micro-/nano-scale building blocks with different constituent materials.

In this work, we devise a hierarchical modular design and fabrication methodology to integrate multiresonant plasmonic nanoantenna arrays on top of micropillar electrode arrays, producing a general class of two-tier protruding micro-/nano-optoelectrode arrays, which feature biomimetic topology and complementary biophotonic-bioelectronic modalities for bioelectrical recording and surface-enhanced Raman spectroscopy (SERS) biochemical detection. The method involves a multilayer lift-off process to create three-dimensional (3D) protruding structures with electrical interconnects and soft interference lithography to create nanohole array deposition masks for patterning metallic-dielectric nanoscale features on hierarchical surfaces. The combination of nanolaminate nanoantennas and conductive micropillars elicits unique optical and electrical characteristics that can be exploited with further

optimization and experimentation. For optical characteristics, the micro-reflectance of a single micro-/nano-optoelectrode shows a double-resonant optical response in the visible/near-infrared window because of the excitation of multiple hybridized plasmonic modes. Stokes inelastic scattering signals from a bound thiol molecule enjoy a six-order of magnitude enhancement due to the nanoantenna's intense near-field enhancement and spectral mode overlap at the laser excitation wavelength. The calculated far-field and near-field optical properties using the finite-difference time-domain (FDTD) method reveal that the measured high SERS enhancement factors ($\approx 10^6$) result from intense localized optical fields due to constructive near-field interference of multipolar plasmonic modes in nanolaminate nanoantennas with their induced image in the metallic mirror ground plane. For electrical characteristics in 1× phosphate-buffered saline, electrochemical impedance measurements show one order of magnitude reduction in the electrochemical impedance due to an increase in electrochemically active surface area compared to a planar electrode. Furthermore, cyclic voltammograms reveal large charging currents for micro-/nano-optoelectrodes compared to planar electrodes due to the more extensive electric double layer (EDL) at the interface between the conductive 3D electrode and aqueous electrolyte, potentially benefiting other applications such as supercapacitors, fuel cells, electroporation devices, and dielectrophoretic devices.[24]

2. Top-down modular fabrication procedure

Fig. 1a illustrates the procedure of fabricating two-tier protruding micro-/nano-optoelectrode arrays in a modularized, scalable, and complementary metal-oxide-semiconductor (CMOS) compatible manufacturing process. A combination of microscale photolithography, phase-shifting lithography, and thin-film physical vapor deposition (PVD) enables the control of the geometry and material processing parameters for micropillars, microelectrodes, and nanoantennas. The nanofabrication procedure begins with the patterning of a superlattice array

of polymeric (SU-8) micropillars (diameter ≈ 2.5 μm, height ≈ 5 μm) on a silicon wafer using direct-write photolithography (DWPL). Alignment markers ensure precise overlap between micropillars and the multi-electrode (MEA) array pattern. Second, we define the microelectrode, contact lines, and contact pads by spin-coating and DWPL of a bilayer resist stack consisting of a nominally 1.3 μm thick positive-tone photoresist and a 500 nm thick lift-off resist on top of the protruding micropillar MEA. Subsequently, an undercut was developed in the bilayer photoresist (PR) stack for thin-film deposition (**Fig. S1**). Third, we deposited approximately ≈30 nm of SiO_2, ≈10 nm of Cr, and ≈100 nm of Au by magnetron sputtering PVD to achieve conformal sidewall coating of micropillars, structurally anchoring the micropillars on each of the microelectrodes with corresponding contact lines and pads for the electrical interface. Fourth, spin-coating and DWPL of an additional PR layer enabled us to mask the entire chip except for the 64 square microelectrode regions, selectively constraining the regions for nanoscale pattern transfer during the PVD process. Next, we transferred onto the chip a precut 1 cm × 1 cm Au film perforated with an ordered nanohole array (AuNHA), which was prefabricated using soft interference lithography[25] with a resultant nominal hole diameter of ≈130 nm and periodicity of ≈ 400 nm (see **Supporting Information** for AuNHA fabrication details). For the transfer process, we lifted off the AuNHA from its carrier substrate, then transferred and resuspended the AuNHA thin-film in a large water-filled glass dish, enabling us to submerge a glass slide (75 mm x 26 mm) and remove the thin-film in a scooping manner. Prior oxygen plasma treatment of the microscope slide resulted in a hydrophilic surface and improved the scooping process. The AuNHA was subsequently transferred onto the micropillars by positioning one edge of the glass slide directly over the center of the wafer with a slight angle and simultaneously using a plastic pipette to provide a stream of water, dragging the thin film from the glass slide onto the wafer. The remaining water underneath the AuNHA was left to evaporate at room temperature. Following the AuNHA transfer, we deposited

alternating layers of Au (nominal thickness = 12 nm) and SiO_2 (nominal thickness = 9 nm) by electron-beam evaporation PVD without substrate rotation to maintain a direct line-of-sight between the sample and crucible. We included Cr (thickness = 1 nm) as an adhesion layer with Au micropillars and Ti (thickness = 0.7 nm) as the interfacial adhesion layers between Au and SiO_2. A 1-methyl-2-pyrrolidone (NMP) based solvent stripper is used to complete the lift-off process and reveal metalized MEA pattern on the silicon wafer. A camera image shows the footprint of the final device, which covers an area of 5 cm × 5 cm on a three-inch silicon wafer (**Fig. 1b**).

We characterize the structural properties at different length scales using micrographs from an optical microscope and scanning electron microscope (SEM). The SEM micrograph in **Fig. 1c** shows a square array of 8 × 8 uniformly patterned microelectrode pads (size: 30 μm × 30 μm, spacing: 100 μm) with contact lines. For a side-by-side comparison, both the planar and 3D optoelectrodes were made using the same 2D mask layout and bilayer lift-off process, ensuring the same areas and thicknesses of the metal layers in the experiments. Before commencing with the fabrication process of both samples, we ensured accurate sputtering thickness control of SiO_2, Cr, and Au by depositing each material separately on the silicon wafers and measuring the thickness using an ellipsometer to calibrate the deposition rates accurately. A top-down SEM image shows a 4 × 4 array of micropillars on each microelectrode pad (**Fig. 1d**). The micropillar height is controlled by the spin-coating thickness of the SU-8 resist, which was nominally 5 μm in our procedure. After several development cycles for different resists in the fabrication process, we observed a decrease in pillar height (≈ 4 μm) with rounded top edges. Magnified SEM images of a single electrode pad reveal highly ordered nanoantenna arrays on the bottom microelectrode pad surface and the top of the protruding micropillars. The inset in **Fig. 1e** shows a top-down view of a single micropillar. To ensure micropillar structural and chemical integrity, we promote complete SU-8 polymer resist cross-

linking by baking the chip on a hot plate at 180 ˚C for 45 min. A closer look at the micropillar top reveals the nanolaminate nanoantennas conformally covering the top surface of the micropillars (**Fig. 1f**). Lastly, a cross-sectional SEM image obtained by focused ion milling (**Fig. 1F inset)** shows the nanolaminate composition of a single nanoantenna with $Au/SiO_2/Au/SiO_2/Au$ multi-layers and a tapered shape due to the shadowing effect of accumulated material around the nanoholes, altering the line-of-sight electron-beam PVD through the AuNHA mask.[26, 27]

3. Optical properties and SERS performance

To characterize the passive optical response of the micro-/nano-optoelectrodes, we used a commercial confocal microscope equipped with a spectrometer in a dual-source configuration to obtain (*i*) single-point micro-reflectance spectral response and (*ii*) average SERS sensing performance and two-dimensional Raman scattering spatial distribution maps from a two-dimensional (2D) slice intersecting the micropillar domes (**Fig. 2**). The reflectance from a planar electrode shows the typical flat metal film response, increasing gradually to ≈ 97 % from 600 nm to 850 nm. In contrast, for the same wavelength span, the reflectance from a single micro-/nano-optoelectrode micropillar exhibits a broadband reduction in intensity by up to ≈ 20 % at 850 nm and spectral dip features at ≈ 690 nm and ≈ 760 nm, manifesting the double-resonant response of plasmonic nanolaminate nanoantennas. For SERS measurements, we disabled the white-light source port used for micro-reflectance measurements and enabled the diode laser source with a wavelength of 785 nm and a nominal average power of 1 mW. Both the planar electrode and micro-/nano-optoelectrode were coated with a non-resonant Raman probe, benzothiazole (BZT), to form a bound monolayer on Au surfaces. The BZT molecule bound to the gold surface on micro-/nano-optoelectrodes exhibits distinct vibrational Raman scattering signatures at 417 cm^{-1}, 1021 cm^{-1}, 1073 cm^{-1}, 1569 cm^{-1}, allowing us to estimate the

SERS enhancement factor (EF) and spatial distribution.[28] The average SERS response of a sputtered planar electrode shows a low wave-number pseudo peak attributed to electronic Raman scattering (ERS) due to the relaxation of momentum conservation by momentum transfer from microscopic surface roughness.[29] However, no discernable Raman scattering signatures are present in the spectra due to the absence of strong local field enhancement to increase the vibrational transition rates of the BZT molecules (**Fig. 2b**). By separating the pixels corresponding to the top pillar plane and bottom pad surfaces of the micro-/nano-optoelectrode array, we find that the overall BZT signal from the top surface is one order of magnitude larger than the BZT signal from the bottom surface, which originates from the effects of off-focus excitation beyond the focal depth and the partially partitioned signal collection from the pinhole in the confocal configuration, allowing normal-incidence reflected light from the background. Beyond Raman scattering signals, we can see an inverse relationship in the linear Rayleigh and nonlinear electronic Raman scattering signals, indicating the depletion of the incident laser energy and reconversion through plasmon-enhanced nonlinear decay channels, evidenced by a larger ERS signal for the in-focus top micropillar regions. Furthermore, the linear Rayleigh scattering signal conveys the reflective (optical path length) differences of the two-tiered micro-/nano-optoelectrode, allowing for the segmentation of the micropillar tops from the bottom pad. Specifically, the average Rayleigh scattering peak was used as a threshold to distinguish between the corresponding top pillar and bottom pad pixels in the 2D Raman maps (**Fig. S2**). Using the average SERS signal from the peak at 1073 cm^{-1} for the top pillar regions, we estimate the SERS EF distribution in the histogram shown in **Fig. 2c** with a mean EF of $\approx (1.56 \pm 1.75) \times 10^6$. The experimental statistical uncertainty is given by one standard deviation above and below the mean value. The source of the uncertainty in the measured BZT signal and subsequently the enhancement factor can arise from (i) variations of BZT molecular orientation due to the curved surface of micropillar tops, (ii) possible surface area competing effects of

residual resist, preventing a uniform self-assembled BZT monolayer coverage, and (iii) differences between the focusing plane and micropillar domes in the 2D area scans. Notably, the scanning procedure entailed focusing on one micropillar dome and maximizing the ERS signal to establish a fixed vertical (z) position of the focal plane for the entire scan, and the 2D area bounds were set using software controls that communicated with an automated piezo stage.

The 2D Raman maps (25 × 25 pixels) in **Fig. 2d (left column)** clearly show the spatial intensity distribution between the top and bottom surface of micro-/nano-optoelectrodes for the electronic Raman scattering (ERS) peak (I_{ERS}) at 79 cm^{-1} and BZT Raman scattering peaks at 417 cm^{-1} (I_{417}) and 1073 cm^{-1} (I_{1073}) with a relative standard deviation (RSD) of ≈110 %. (Note: RSD = $\sigma/\mu \times 100$ %, where σ is the standard deviation, and μ is the mean.) Such broad RSD manifests the SERS measurement variations in plasmonic nanoantenna geometries and laser excitation focus conditions, making quantitative SERS analysis difficult. Our recent research has shown that plasmon-enhanced ERS signals from metal can serve as an internal standard for spatial and temporal SERS calibration[30]. As shown in **Fig. 3d (right column)**, the ERS-calibrated 2D SERS maps for I_{417}/I_{ERS} and I_{1073}/I_{ERS} exhibit a much-reduced RSD from ≈100 % and ≈110 % to ≈12 % and ≈13 %, comparable to the I_{417}/I_{1073} RSD value of ≈14 % by self-calibration between two vibration modes of the BZT molecule. After the ERS calibration, the slight spatial uniformity in 2D SERS maps is likely due to Raman scattering cross-section variations from inhomogeneous molecule orientation arrangement in the surface-modified BZT monolayer. We envision that ERS calibration can significantly improve quantitative SERS biochemical analysis of molecule concentrations from the top and bottom surface of micro-/nano-optoelectrodes for future bio-sensing applications.

4. Numerical analysis of microscopic mode characteristics

To understand the measured far-field response in the context of microscopic near-field interactions from plasmon excitation, we use numerical finite-difference-time-domain (FDTD)

simulations to calculate the far and near-field optical response with a model of the micro-/nano-optoelectrode based on the estimated dimensions from the SEM images shown in Fig. 1 and **Fig. S1** (see **Supporting Information**). SEM images clearly show nanoantenna size variation on the micropillar domes. Hence, to better understand the size-dependent optical response, we calculate the reflectance spectra for a select range of radii, matching estimates from SEM images including r = 62 nm, 66 nm, and 70 nm (**Fig. 3a**). FDTD calculated far-field plots reveal several distinct characteristics of micro-/nano-optoelectrode. First, consistent with the measurements in **Fig. 2a**, the planar electrode shows a high reflectance in a wavelength range of 600 nm to 850 nm due to a low penetration depth of optical fields into the metal (**Fig. 3a**). Second, in agreement with measurements, FDTD calculated reflectance spectra of the micro-/nano-optoelectrode show a broadband absorption from 600 nm to 850 nm with two resonant modes at λ_1 and λ_2. Third, the micro-/nano-optoelectrode reflectance spectral reveals that the λ_1 mode remains fixed in spectral position ($\approx$ 640 nm) and reflectance when increasing nanoantenna base radius from r = 62 nm to r = 70 nm, whereas the λ_2 mode redshifts from 730 nm to 810 nm with a correspondingly larger dip in reflectance. The measurements also reveal such double-resonant characteristics of micro-/nano-optoelectrode with two spectral dips at $\approx$ 690 nm and $\approx$ 760 nm (**Fig. 2a**). Differences between the measurement and simulation can be attributed to fabrication-related surface roughness, homogenous and inhomogeneous broadening effects, and plasmon damping from interfacial 1 nm thick Cr adhesion layer between Au and SiO_2.[31]

To investigate the microscopic nature of the modes supported in micro-/nano-optoelectrodes, we calculate the near-field distribution maps of normalized intensity ($|E|^2$ and $|H|^2$) and phase ($\varphi(E_z)$, $\varphi(E_x)$, $\varphi(H_y)$) for the two modes at $\lambda_1 \approx 640$ nm (**Fig. 3b**) and $\lambda_2 \approx 785$ nm (**Fig. 3c**) in micro-/nano-optoelectrodes with r = 66 nm. The 2D near-field plots

reveal several distinct mode characteristics that differ from the same nanoantenna arrangement without the conductive micropillar (ground plane) (**Fig. S4** in **Supporting Information**). First, **Fig. 3b** shows that the λ_1 mode exhibits (*i*) electric dipole (ED) characteristics with an in-phase $\varphi(E_x)$ distribution in three Au nanodisks except for an out-phase $\varphi(E_x)$ in the bottom nanodisk extended below the metal surface and (*ii*) weak magnetic response within and around the nanoantenna shown in the $|H|^2$ distribution map. As a comparison, the λ_1 mode in the nanoantenna with ground plane shows a substantial suppression of intensity (normalized $|E|^2$ $<10^2$), while the λ_1 mode in the nanoantenna without a ground plane (in the air) support enhanced intensity (normalized $|E|^2 > 10^3$) to penetrate into the dielectric gap nanocavities (**Fig. S4** in **Supporting Information**). Next, the near-field plot of the mode at λ_2 = 785 nm reveals (*i*) magnetic dipole (MD) characteristics with high magnetic fields in both bottom and top nanocavities and in-phase $\varphi(H_y)$ in and below the nanoantenna, and (*ii*) electric quadrupole (EQ) characteristics where the top and middle Au nanodisks show an out-of-phase $\varphi(E_x)$ distribution compared to the bottom Au nanodisk (**Fig. 3c**). Furthermore, spatially distributed magnetic fields that extend below the nanostructure are not observed for nanoantennas in the air (**Fig. S4** in **Supporting Information**), revealing the ground-plane loading effects from the conductive surfaces that provide an additional degree of mode engineering by mirror-mode coupling.[32-34] Lastly, we can see the large intensity region (normalized $|E|^2 > 10^3$) uniformly distributed within and around the top and bottom nanocavities, indicating that image-induced coupling affects the microscopic characteristics for the λ_2 mode, including an enhanced optical field intensity, spatial distribution, and magnetic response.[35]

Fig. 3d illustrates the interaction of the ED mode in the nanolaminate nanoantenna with its image in the ground plane (highly conductive surface), where the electric dipole parallel to the surface couples with its out-of-phase mirror image electric dipole to generate a bonding EQ

mode with reduced optical cross-section and red-shifted resonant wavelength. **Fig. 3e** illustrates the interaction of the MD mode in the nanolaminate nanoantenna with its image in the ground plane, where the magnetic dipole couples with its in-phase mirror image magnetic dipole to generate an antibonding MD mode with the increased optical cross-section and blue-shifted resonant wavelength.[36] Furthermore, FDTD calculations reveal that a nanolaminate nanoantenna on the ground plane can support a lower energy magnetic quadrupole (MQ) mode around 1000 nm with an increased optical cross-section than the case in air (without a ground plane) (**Fig. S4** in **Supporting Information**), manifesting that a magnetic quadrupole can constructively interact with its image in the mirror, altering the intrinsic radiation properties via an antenna loading effect analogous to its radio-frequency counterpart.[37]

5. Measured electrode properties

To understand the potential interfacial dynamics that can influence electrode electrochemical (EC) characteristics in biological solutions, we used 1× PBS with a nominal pH of ≈7.4 to mimic similar osmolarity and ion concentration typically found in isotonic physiological conditions. Using a custom EC-cell, we conducted electrochemical impedance spectroscopy (EIS) and cyclic voltammetry (CV) to probe the double-layer capacitance and diffusion characteristics at the electrode-electrolyte interface (**Fig. 4**). The average response of individual EIS spectra is measured from three randomly picked electrode units. Every electrode spectrum consists of ten frequency points per decade averaged from ten measures per frequency. As shown in **Fig. 4a-b**, the solid line is the mean spectrum, and the shaded region represents the one standard deviation statistical uncertainty. The relative uncertainty in the impedance magnitude and phase is larger for micro-/nano-optoelectrode than for the planar electrode, indicating the sensitive dependence of the interfacial electrochemical behaviors on micro-/nano-structured surface topology. Geometrical variations of surface topology for different

micro-/nano-optoelectrodes can be attributed to the partial misalignment between the nanoantenna array and electrode 2D spatial area, as shown in **Fig. S1a (Supporting Information)**. However, with an overall increase in surface area, micro-/nano-optoelectrodes exhibit an order-of-magnitude reduction in impedance magnitude ($|Z|$) compared to the planar electrode in a frequency range of 1 Hz to 100 kHz. Specifically, for the typical action potential frequency around 1 kHz, $|Z|$ reduces from 60 kΩ for the planar electrode to 5 kΩ for the micro-/nano-optoelectrode (**Fig. 4a**), manifesting the inverse dependence of impedance on surface area ($Z \propto A^{-1}$) due to the hierarchical geometry.[38]

Next, the impedance phase plot reveals three distinct regions within the frequency spectrum from 1 Hz to 100 kHz where micro-/nano-optoelectrodes differ distinctly from the planar electrode (**Fig. 4b-c**). In the low-frequency band between 1 Hz and 10 Hz, the micro-/nano-optoelectrode has a larger phase (–60°) than the planar electrode (–90°), indicating diffusion-limited ion transfer current and modified interfacial ionic double layer in hierarchical geometries.[39] In the intermediate-frequency band between 100 Hz and 1 kHz, the planar electrode shows an increased phase from –90° to –45°; in contrast, the micro-/nano-optoelectrode exhibits a reverse trend with a reduced phase from –60° to –85°, revealing a transition of the dominant current from the longer-range ion diffusion to the short-range charging-discharging in the electric double-layer capacitor (EDLC).[40] In the high-frequency band between 10 kHz and 100 kHz, the phase for the planar and micro-/nano-optoelectrode is –90° and –30°, respectively, revealing another reversal in characteristics where the planar electrode now behaves as an EDLC while the response of micro-/nano-optoelectrode is affected by ion transport limitation and non-uniform pathway for ion transport from the bulk electrolyte.[40, 41]

Fig. 4c shows the CV curves in a decadic logarithm scale to illustrate the magnitude differences in the current response between planar and micro-/nano-optoelectrodes (linear CV

plot reproduced in **Supporting Information**). With a relatively slow scan rate of 50 mV/s, the CV measurements can approach a quasi-static electrochemical interface in the low-frequency limit. Under the applied working electrode potential from –0.6 V to 0.6 V, the planar electrode generates a current response between -10^{-5} A and 10^{-5} A, while the micro-/nano-optoelectrode produces a two-order of magnitude higher current response between -10^{-3} A and 10^{-3} A. Compared to the planar electrodes, the increased surface area of micro-/nano-optoelectrode contributes to a larger EDLC, as indicated by the larger area enclosed in the voltammogram trace.[42]

6. Nyquist plot and equivalent circuit modeling

To better understand the enhancement of electrochemical performances by introducing the micro-/nano-structures, we have performed an equivalent circuit model simulation to analyze and fit the measured Nyquist impedance plots (**Fig. 5)**. By decomposing the real and imaginary parts of the measured impedance in a Nyquist plot, shown as black and red circles in **Fig. 5a**, we can extrapolate the general resistive (real part) and capacitive reactance (negative of the imaginary part) characteristics of planar electrode and micro-/nano-optoelectrode impedance. First, in the low-frequency regime between 1 Hz to 10 Hz (1 Hz is the first data point furthest from the origin), the planar electrode shows a more significant slope with larger capacitance (≈ 8x). In contrast, micro-/nano-optoelectrodes show a smaller slope near unity, indicating that the 3D geometry of micro-/nano-optoelectrode affects the diffusion-related mass transport processes in the low-frequency limit and thus the equilibrium differential capacitance.[40] Also, we should note that the unity slope in micro-/nano-optoelectrode does not necessarily suggest an ideal semi-infinite planar electrode case since our EC cell has a finite volume with additional impedance from the connection and substrate components. On the contrary, the slope of the planar electrode in the low-frequency limit turns out to be much larger than one, which is due

to the reasons above. Second, in the intermediate frequency (100 Hz to 1 kHz), while the planar electrode shows a rapid slope decrease with frequency, micro-/nano-optoelectrodes show a gradual increase in slope with the frequency, indicating that non-overlapped diffusion layers of adjacent micropillars can contribute to increased capacitive attributes.[39, 43] Third, in the high-frequency regime (10 kHz to 100 kHz), while the slope of the planar electrode increases to a vertical trend, the slope of the micro-/nano-optoelectrode increases then plateaus slightly, manifesting changes to a compact EDLC at the interface, likely due to ion mobility limits at high-frequencies.

We select the electrical circuit modeling elements to fit the measured Nyquist plots by considering several interfacial processes for microscopic anions, cations, and water molecules at the electrode-electrolyte interface during electrochemical equilibrium with a zero direct current. Notably, the general electrode-electrolyte interface consists of three spatial regions, including rigid layer, diffuse layer, and undisturbed electrolyte, which can be modeled with corresponding lumped circuit elements in **Fig. 5c.** First, a layer defined as the inner Helmholtz plane is established from the hydration of the metal surface with polar water molecules due to the electrostatic attraction to excess surface charges. There are rigidly held counterions on the water layer that resist thermal motion, which define the outer Helmholtz plane represented as red circles for sodium and potassium cations in PBS in **Fig. 5b**. The rigidly held counterions separated by water molecules from the metal surface charges comprise the first electrochemical structure, which is known as the rigid layer (or Helmholtz double layer). A constant phase element (CPE) can model the rigid layer to account for variations in the orientation polarization of water molecules, resulting in an electrochemical equivalent of a leaky capacitor with an imperfect dielectric layer.[44] The impedance of the CPE is expressed as, $Z_{CPE}(f) = \frac{1}{Q(j2\pi f)^{\beta}}$, where Q is the CPE (nonideal capacitance) with units $F \cdot s^{\beta - 1}$ $where\ s = j2\pi f$, f is the

frequency in Hertz, $j = \sqrt{-1}$, and $\beta \in [0,1]$ is an ideality factor (note: β = 1 yields the impedance of an ideal capacitor).[45] Intercalation of specifically adsorbed anions (chloride ions, blue circles) within the inner Helmholtz plane is also possible due to short-range chemical adhesive forces, *e.g.*, Van der Waals interactions, leading to direct bonding to the metal surface where local chemical bonding forces are not saturated because of the local specific crystallographic structure or due to local defects of the crystal lattice.[44] Beyond the rigid layer, other counterions (space charges) are mobile, collectively constructing a cloud of space charge defined as the diffuse layer (or Gouy-Chapman double layer) with a thickness defined as the Debye length. Conventionally, within the diffuse region, we can use a semi-infinite linear diffusion Warburg element (W_d) to account for diffusion from spatial concentration gradients of the different dissolved ions in the electrolyte.[44] The Warburg element (W_d) can build on the constant phase element, $Z_{CPE}(f) = \frac{1}{Q(j2\pi f)^{\beta}}$, by setting β=0.5. Current in the diffuse regions can travel through two pathways. The first pathway mediates the faradic current through the Warburg element (W_d) and charge-transfer resistance (R_{ct}). The second pathway mediates the non-faradic current associated with the charging and discharging of the Gouy-Chapman double-layer capacitance (C_d). Since the EIS measurements are performed in PBS, an inert electrolyte without redox-active species, the direct charge transfer between the electrode-electrolyte interface is relatively small, resulting in a dominant non-faradic current pathway in the current model.[40] Therefore, the charge-transfer resistance in this context is likely due to the adsorption and desorption processes of monolayer Cl- ions on the Au surface, which can contribute to a small Faradaic current.[46] The third and last region is the undisturbed electrolyte layer, where cation and anion concentrations are equal and can be modeled with electrolyte resistance (R_e), which may also include parasitic contact and equipment resistance contributions in the circuit.

The circuit model parameters used to fit the measured Nyquist plot in **Fig. 5a** were obtained by the Levenberg-Marquardt minimization algorithm, which was based on yielding the lowest $\chi^2/|Z|$ value, resulting in 0.012 Ω and 0.038 Ω, respectively, for the planar and micro-/nano-optoelectrode. The weighted $\chi^2/|Z|$ is an indicator of goodness of fit and estimates the distance between the measured data and the simulated data. The expression is given by, $\chi^2/|Z| = \sum_{i=1}^{N} |Z_i(f_i) - Z(f_i)|^2/|Z(f_i)|$ where Z_i is the measured impedance and $Z(f_i)$ is the value of the impedance calculated at a frequency f_i for a defined set of circuit parameter values and the number of points N of the iterated minimization algorithm. The minimization process yields the corresponding circuit parameters, shown in **Fig. 5d**, with a deviation parameter. The deviation (dev) parameter can be assimilated to a standard deviation, and it conveys an estimate of the relevancy of the parameter, i.e., if dev is relatively large, then its variation in value will not affect the quality of the fit, rendering it uncritical in the minimization process, and indicating that the circuit needs simplification or the physical basis for the circuit model is invalid. Therefore, the dev parameter can assess the uncertainty in the circuit model's ability to recapitulate the underlying frequency-dependent impedance dynamics from the microscopic electrode-electrolyte interfacial processes. As was previously the case for **Fig. 5a**, there is an uncertainty in the surface area and topology of different 3D electrodes, resulting in a unique set of circuit parameters for each 3D electrode, but the circuit model generally remains applicable to all. We extract the component values from the equivalent circuit model fit to reveal several unique characteristics. First, we find that the R_{ct} value for micro-/nano-optoelectrodes (R_{ct}≈190 kΩ, dev ≈ 17 Ω) is higher than planar electrodes (R_{ct} ≈ 81 kΩ, dev ≈ 2.7 Ω) despite their larger surface area, which is likely due to the slight polymer residue on micro-/nano-optoelectrodes from extra photoresist spin-coating involved nanofabrication processes. Second, the Warburg parameter for micro-/nano-optoelectrodes ($W_d \approx 1\ M\Omega \cdot s^{-0.5}$, dev ≈ $75\ \Omega \cdot s^{-0.5}$) has a larger

value than planar electrodes ($W_d \approx 0.4\ M\Omega \cdot s^{-0.5}$, dev ≈ $60\ \Omega \cdot s^{-0.5}$), suggesting that their larger diffusive layer thickness contributes to a decrease in capacitance offset by an increase in surface area. Third, the double-layer capacitance for micro-/nano-optoelectrodes ($C_d \approx 49$ nF, dev ≈ 6×10^{-3} nF) is one order larger than planar electrodes ($C_d \approx 6$ nF, dev ≈ 2×10^{-3} nF), revealing that the total surface area plays a more significant role while the larger diffusive layer thickness is less significant to affect the total double-layer capacitance. Next, the thickness of the rigid layer is constrained by the effective radius of solvated counterions (≈ 0.1 nm), so the one-order in magnitude increase in Q_r from $\approx 21\ nF \cdot s^{\beta-1}$ (dev ≈ $4 \times 10^{-6}\ nF \cdot s^{\beta-1}$) to $\approx 350\ nF \cdot s^{\beta-1}$(dev $\approx 1 \times 10^{-2}\ nF \cdot s^{\beta-1}$) is mainly due to increased surface area and effective surface roughness between planar electrodes and micro-/nano-optoelectrodes. Compared to the planar electrode with $\beta = 0.97$, resembling the ideal capacitor, the micro-/nano-optoelectrode with $\beta = 0.81$ shows a nonideal capacitance behavior due to its micro-/nanostructured surface inhomogeneities within the inner Helmholtz plane, where the distribution and dipole moment orientation for water molecules, and surface adsorbed anions/cations can vary significantly at different locations.[47] Lastly, R_e for micro-/nano-optoelectrode ($R_e \approx 200\ \Omega$, dev ≈ 0.3 Ω) is larger than the planar electrode ($R_e \approx 90\ \Omega$, dev ≈ 0.4 Ω), which may be associated with the different distances between their working and counter electrodes in the EC-cell.

7. Conclusion

A top-down modular fabrication procedure was developed to pattern nanolaminate nanoantennas on micropillar electrode arrays, enabling tunable hybrid optical-electrical functionality in a single device. Optical and electrical functionality dependent on structural geometry can be tuned by controlling design and processing parameters such as micropillar diameter and PVD deposition thickness. Experimental and calculated far-field optical spectra reveal multiple resonant plasmonic modes. Our calculated near-field 2D maps show that

nanolaminate nanoantennas on the ground plane can enjoy enhanced magnetic field intensities within dielectric nanocavities due to the interactions with its image mode as a result of the ground-plane-like loading effect.[48] Electrochemical impedance spectroscopy and cyclic voltammetry provided insights into area-dependent microscopic electrochemical dynamics at the electrode-electrolyte interface with unique characteristics that warrant further investigation. We envision that micro-/nano-optoelectrode arrays can serve as a multifunctional platform for monitoring and modulating cellular systems. Specifically, the proposed system-level modular design method can overcome challenges in achieving tight cell-device coupling and optimized hybrid device properties for achieving multimodal bioelectrical recording and SERS biochemical analyses with minimal perturbation to intrinsic cellular functions. Lastly, the proposed design approach can be generalized to incorporate 3D printing of micro-/nano-scale templates using stereolithography or 2-photon lithography to further expand the design space of complex 2D and 3D patterns for hierarchically structured micro-/nano-optoelectrodes. Such a focus on modularized design and fabrication will facilitate the systematic development of multimodal bio-machine interfacing systems for biological and medical applications using chip-based or flexible mesh-based substrates.

8. Author Contributions

EM developed the final device and performed optical and electrochemical measurements with corresponding FDTD and equivalent circuit models. JS fabricated the AuNHA. YZ and CX assisted EM with electrochemical measurements. YQ assisted with FDTD simulations. AA and WZ advised EM.

9. Conflicts of Interest

There are no conflicts to declare.

10. Acknowledgement

This work was supported by US AFOSR Young Investigator Award FA9550-18-1-0328, US AFOSR DURIP Award FA9550-19-1-0287, US NIST grant 70NANB18H201, and US NIST grant 70NANB19H163. EM conducted the device fabrication with support from the NIST summer undergraduate research fellowship (SURF) in 2019, and EM is immensely grateful for the mentorship, training, and advice received from NIST staff, including Kerry Siebein, Stoyan Jeliazkov, B. Robert Ilic, Chen (Jessie) Zhang, and Gerard Henein.

Disclaimer: Certain commercial equipment, instruments, or materials are identified in this paper to foster understanding. Such identification does not imply recommendation or endorsement by the National Institute of Standards and Technology, nor does it imply that the materials or equipment identified are necessarily the best available for the purpose.

Figures

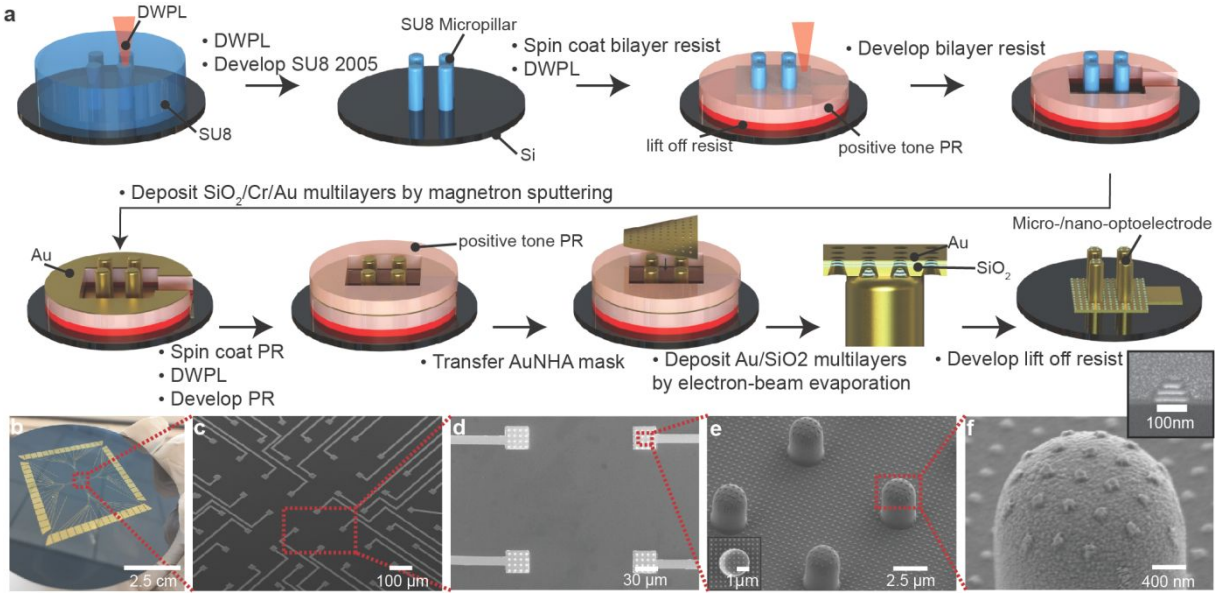

Fig. 1 Wafer-scale two-tier protruding micro-/nano-optoelectrode arrays by hierarchical modular design. (a) Schematic illustration of the fabrication process. DWPL: direct write photolithography, PR: photoresist (b) Camera image of the wafer-scale sample. (c) Perspective SEM image of microelectrode pad arrays (pad size: 30 × 30 μm^2) with contact lines. (d) The top-down SEM image shows that each microelectrode pad consists of a 4 × 4 array of protruding micropillar electrodes (diameter ≈ 2.5 μm, height ≈ 5 μm). (e) The perspective and (f) magnified SEM images show that each protruding micropillar electrode consists of Au/SiO_2/Au/SiO_2/Au nanolaminate nanoantenna arrays on the top. The inset of **Fig. 1e** illustrates the cross-sectional SEM image of a nanolaminate nanoantenna.

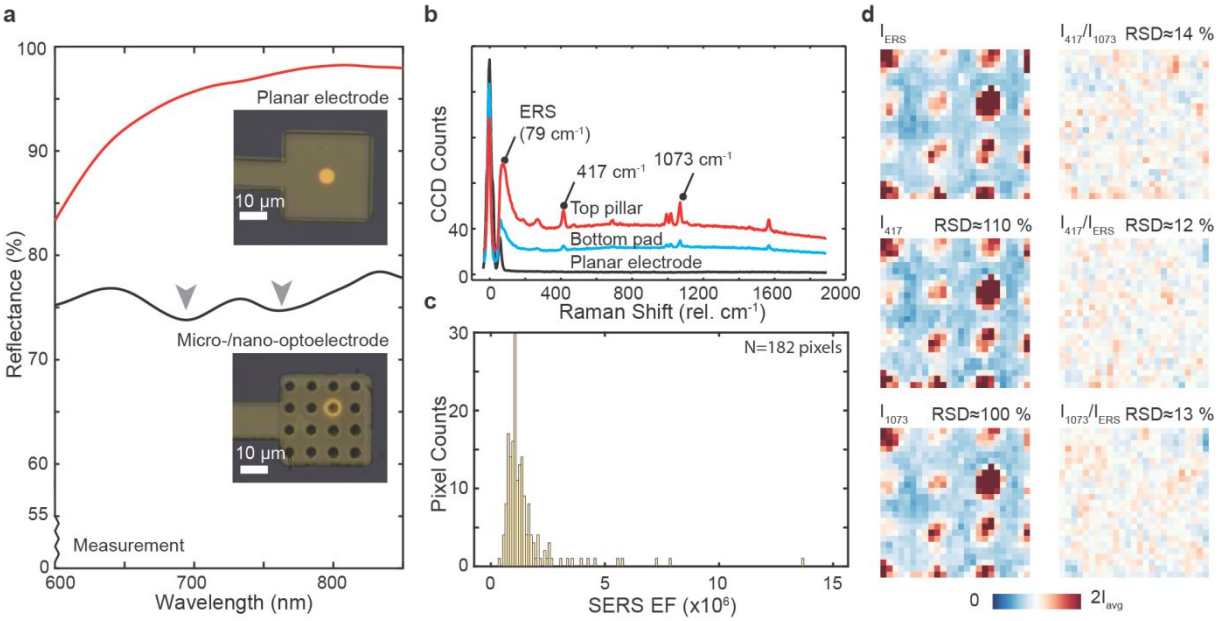

Fig. 2 Optical properties and SERS performance. (a) Measured micro-reflectance spectra of the micro-/nano-optoelectrodes and the planar electrode. (b) Measured Raman spectra of BZT molecules from the top and bottom surface of micro-/nano-optoelectrodes and the planar electrode (averaged from 625 total pixels). For clarity, the spectra are offset in the *y*-axis by 10 charge-coupled device (CCD) counts. (c) Histogram of Raman signal intensities and the corresponding SERS enhancement factor (EF) for 1073 cm^{-1} BZT peak from the top surface of micro-/nano-optoelectrodes. (d) 2D Raman mapping images of I_{ERS} at 79 cm^{-1}, I_{417} at 417 cm^{-1}, I_{1073} at 1073 cm^{-1}, I_{417}/I_{ERS}, I_{1073}/I_{ERS}, and I_{417}/I_{1073} with the scale normalized between 0 and $2I_{avg}$.

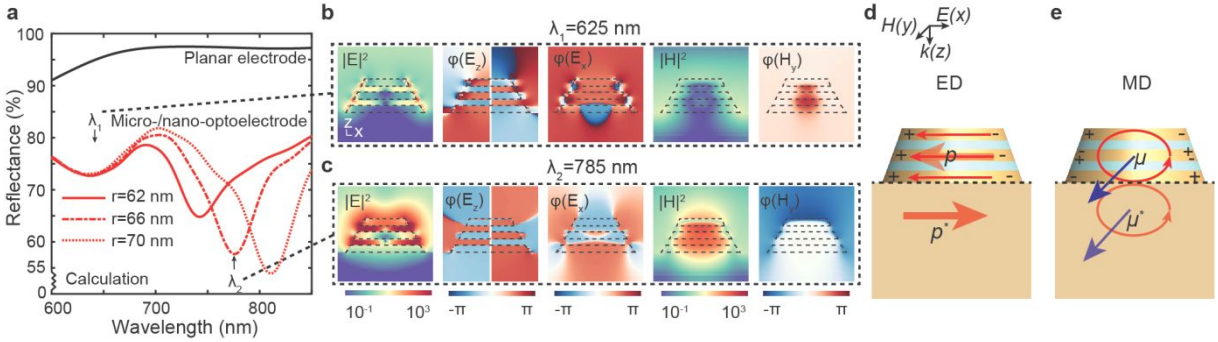

Fig. 3 Microscopic multiresonant behaviors with loading effects of the metal ground plane. (a) FDTD calculated reflectance spectra of the micro-/nano-optoelectrodes with different nanoantenna diameters compared to the planar electrode. (b) FDTD calculated near-field distribution maps of normalized $|E|^2$, $\varphi(E_z)$, $\varphi(E_x)$, $|H|^2$, and $\varphi(H_y)$ in the *x*-*z* plane for resonant modes at λ_1 = 625 nm and (c) λ_2 = 785 nm. (d) Microscopic scheme of λ_1 mode due to destructive interference of electric dipole (ED) mode in nanolaminate nanoantennas and its out-of-phase image ED in the ground mirror plane. (e) Microscopic scheme of λ_2 mode due to constructive interference of magnetic dipole (MD) mode in nanolaminate nanoantennas and its in-phase image MD in the ground mirror plane.

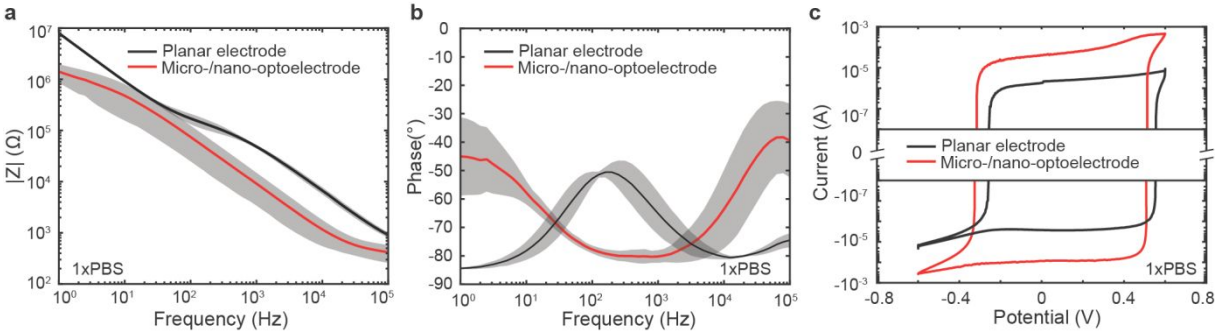

Fig. 4 Electrode properties from electrochemical impedance spectroscopy (EIS) and cyclic voltammetry (CV) measurements. (a) Measured impedance magnitude |*Z*| spectra, (b) measured bode phase plot with the marked (shaded) experimental statistical uncertainties being one standard deviation, and (b) measured voltammogram in log scale for the micro-/nano-optoelectrodes and the planar electrode in 1× phosphate-buffered saline (1× PBS).

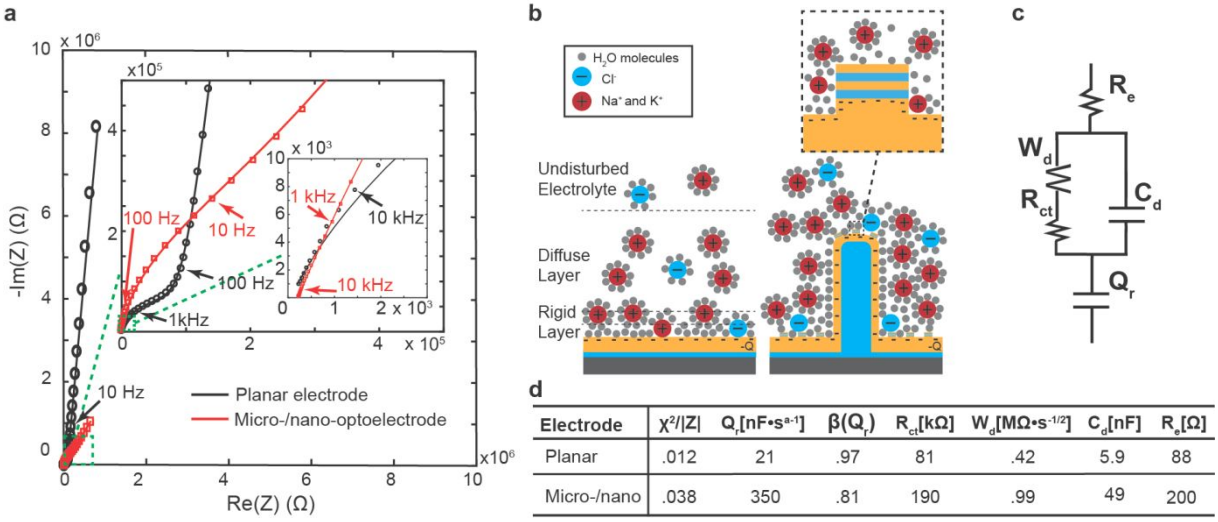

d

Electrode	$\chi^2/\|Z\|$	Q_r[nF•s^{a-1}]	$\beta(Q_r)$	R_{ct}[kΩ]	W_d[MΩ•s$^{-1/2}$]	C_d[nF]	R_e[Ω]
Planar	.012	21	.97	81	.42	5.9	88
Micro-/nano	.038	350	.81	190	.99	49	200

Fig. 5 Nyquist plot and circuit modeling. (a) Measured Nyquist plots and fitted curves based on circuit modeling for the micro-/nano-optoelectrode and the planar electrode in 1× PBS. The inset shows the high-frequency components of the Nyquist plots. (b) Schematic illustration of electrode-electrolyte interface. (c) Equivalent circuit model. (d) The table of fitted results for components used in the equivalent circuit model.

11. References

1. T. A. Dixon, T. C. Williams and I. S. Pretorius, *Nature Communications*, 2021, **12**, 388.
2. M. Nuriya, S. Fukushima, A. Momotake, T. Shinotsuka, M. Yasui and T. Arai, *Nature Communications*, 2016, **7**, 11557.
3. X. Duan, R. Gao, P. Xie, T. Cohen-Karni, Q. Qing, H. S. Choe, B. Tian, X. Jiang and C. M. Lieber, *Nature Nanotechnology*, 2012, **7**, 174-179.
4. C. Xie, Z. Lin, L. Hanson, Y. Cui and B. Cui, *Nature Nanotechnology*, 2012, **7**, 185-190.
5. J. Abbott, T. Y. Ye, L. Qin, M. Jorgolli, R. S. Gertner, D. Ham and H. Park, *Nature Nanotechnology*, 2017, **12**, 460-466.
6. W. Zhao, L. Hanson, H.-Y. Lou, M. Akamatsu, P. D. Chowdary, F. Santoro, J. R. Marks, A. Grassart, D. G. Drubin, Y. Cui and B. Cui, *Nature Nanotechnology*, 2017, **12**, 750-756.
7. M. Dipalo, G. C. Messina, H. Amin, R. La Rocca, V. Shalabaeva, A. Simi, A. Maccione, P. Zilio, L. Berdondini and F. De Angelis, *Nanoscale*, 2015, **7**, 3703-3711.
8. R. La Rocca, G. C. Messina, M. Dipalo, V. Shalabaeva and F. De Angelis, *Small*, 2015, **11**, 4632-4637.
9. V. Caprettini, J.-A. Huang, F. Moia, A. Jacassi, C. A. Gonano, N. Maccaferri, R. Capozza, M. Dipalo and F. De Angelis, *Advanced Science*, 2018, **5**, 1800560.
10. J.-A. Huang, V. Caprettini, Y. Zhao, G. Melle, N. Maccaferri, L. Deleye, X. Zambrana-Puyalto, M. Ardini, F. Tantussi, M. Dipalo and F. De Angelis, *Nano Letters*, 2019, **19**, 722-731.
11. M. E. J. Obien, K. Deligkaris, T. Bullmann, D. J. Bakkum and U. Frey, *Frontiers in Neuroscience*, 2015, **8**, 423.
12. J. Abbott, T. Ye, K. Krenek, R. S. Gertner, S. Ban, Y. Kim, L. Qin, W. Wu, H. Park and D. Ham, *Nature Biomedical Engineering*, 2020, **4**, 232-241.
13. M. E. Spira and A. Hai, *Nature Nanotechnology*, 2013, **8**, 83-94.
14. C. Xie, J. Liu, T.-M. Fu, X. Dai, W. Zhou and C. M. Lieber, *Nature Materials*, 2015, **14**, 1286-1292.
15. X. Dai, W. Zhou, T. Gao, J. Liu and C. M. Lieber, *Nature Nanotechnology*, 2016, **11**, 776-782.
16. A. Hai, J. Shappir and M. E. Spira, *Nat Methods*, 2010, **7**, 200-U250.
17. A. Hai, Ada Dormann, Joseph Shappir, Shlomo Yitzchaik, Carmen Bartic, Gustaaf Borghs, J. P. M. Langedijk, and Micha E. Spira., *Journal of The Royal Society Interface*, 2009, **6**, 1153–1165.
18. J. Langer, D. Jimenez de Aberasturi, J. Aizpurua, R. A. Alvarez-Puebla, B. Auguié, J. J. Baumberg, G. C. Bazan, S. E. J. Bell, A. Boisen, A. G. Brolo, J. Choo, D. Cialla-May, V. Deckert, L. Fabris, K. Faulds, F. J. García de Abajo, R. Goodacre, D. Graham, A. J. Haes, C. L. Haynes, C. Huck, T. Itoh, M. Käll, J. Kneipp, N. A. Kotov, H. Kuang, E. C. Le Ru, H. K. Lee, J.-F. Li, X. Y. Ling, S. A. Maier, T. Mayerhöfer, M. Moskovits, K. Murakoshi, J.-M. Nam, S. Nie, Y. Ozaki, I. Pastoriza-Santos, J. Perez-Juste, J. Popp, A. Pucci, S. Reich, B. Ren, G. C. Schatz, T. Shegai, S. Schlücker, L.-L. Tay, K. G. Thomas, Z.-Q. Tian, R. P. Van Duyne, T. Vo-Dinh, Y. Wang, K. A. Willets, C. Xu, H. Xu, Y. Xu, Y. S. Yamamoto, B. Zhao and L. M. Liz-Marzán, *ACS Nano*, 2020, **14**, 28-117.
19. S.-Y. Ding, J. Yi, J.-F. Li, B. Ren, D.-Y. Wu, R. Panneerselvam and Z.-Q. Tian, *Nature Reviews Materials*, 2016, **1**, 16021.
20. Q. Ge, Z. Li, Z. Wang, K. Kowsari, W. Zhang, X. He, J. Zhou and N. X. J. I. J. o. E. M. Fang, 2020, **2**, 022004.

21. V. Harinarayana and Y. C. Shin, *Optics & Laser Technology*, 2021, **142**, 107180.
22. S. M. Lubin, W. Zhou, A. J. Hryn, M. D. Huntington and T. W. Odom, *Nano Letters*, 2012, **12**, 4948-4952.
23. W. Zhou, H. W. Gao and T. W. Odom, *Acs Nano*, 2010, **4**, 1241-1247.
24. S. Zhang, Z. Zhang, S. Chen and R. Zhu, *Analytical Chemistry*, 2021, **93**, 5882-5889.
25. J. Henzie, M. H. Lee and T. W. Odom, *Nature Nanotechnology*, 2007, **2**, 549-554.
26. E. Mejia, Y. Qian, S. A. Safiabadi Tali, J. Song and W. Zhou, *Applied Physics Letters*, 2021, **118**, 241108.
27. J. Song and W. Zhou, *Nano Letters*, 2018, **18**, 4409-4416.
28. T. H. Joo, M. S. Kim and K. Kim, *J. Raman Spectrosc.*, 1987, **18**, 57-60.
29. M. Inagaki, T. Isogai, K. Motobayashi, K.-Q. Lin, B. Ren and K. Ikeda, *Chemical Science*, 2020, **11**, 9807-9817.
30. W. Nam, Y. Zhao, J. Song, S. Ali Safiabadi Tali, S. Kang, W. Zhu, H. J. Lezec, A. Agrawal, P. J. Vikesland and W. Zhou, *The Journal of Physical Chemistry Letters*, 2020, **11**, 9543-9551.
31. S. J. Madsen, M. Esfandyarpour, M. L. Brongersma and R. Sinclair, *ACS Photonics*, 2017, **4**, 268-274.
32. A. Rose, T. B. Hoang, F. McGuire, J. J. Mock, C. Ciracì, D. R. Smith and M. H. Mikkelsen, *Nano Letters*, 2014, **14**, 4797-4802.
33. J. J. Mock, R. T. Hill, A. Degiron, S. Zauscher, A. Chilkoti and D. R. Smith, *Nano Letters*, 2008, **8**, 2245-2252.
34. Y. Huang, L. Ma, M. Hou, J. Li, Z. Xie and Z. Zhang, *Scientific Reports*, 2016, **6**, 30011.
35. S. Chen, Y. Zhang, T.-M. Shih, W. Yang, S. Hu, X. Hu, J. Li, B. Ren, B. Mao, Z. Yang and Z. Tian, *Nano Letters*, 2018, **18**, 2209-2216.
36. R. R. Chance, A. Prock and R. Silbey, *Physical Review A*, 1975, **12**, 1448-1452.
37. A. Alù and N. Engheta, *Physical Review Letters*, 2008, **101**, 043901.
38. R. C. Gesteland, B. Howland, J. Y. Lettvin and W. H. Pitts, *Proceedings of the IRE*, 1959, **47**, 1856-1862.
39. R. Prehn, L. Abad, D. Sánchez-Molas, M. Duch, N. Sabaté, F. J. del Campo, F. X. Muñoz and R. G. Compton, *Journal of Electroanalytical Chemistry*, 2011, **662**, 361-370.
40. B.-A. Mei, O. Munteshari, J. Lau, B. Dunn and L. Pilon, *The Journal of Physical Chemistry C*, 2018, **122**, 194-206.
41. D. Sánchez-Molas, J. P. Esquivel, N. Sabaté, F. X. Muñoz and F. J. del Campo, *The Journal of Physical Chemistry C*, 2012, **116**, 18831-18846.
42. D. Decker, R. Hempelmann, H. Natter, M. Pirrung, H. Rabe, K. H. Schäfer and M. Saumer, *Advanced Materials Technologies*, 2019, **4**, 1800436.
43. C. Chen, B. Ran, Z. Wang, H. Zhao, M. Lan, H. Chen and Y. Zhu, *RSC Advances*, 2020, **10**, 41110-41119.
44. E. Kaniusas, *Biomedical Signals and Sensors III, Linking Electric Biosignals and Biomedical Sensors*, Springer Publishing, 2019.
45. A. R. C. Bredar, A. L. Chown, A. R. Burton and B. H. Farnum, *ACS Applied Energy Materials*, 2020, **3**, 66-98.
46. T. Hezard, L. Laffont, P. Gros, P. Behra and D. Evrard, *Journal of Electroanalytical Chemistry*, 2013, **697**, 28-31.
47. J. Wu, *Chemical Reviews*, 2022, **122**, 10821-10859.
48. S. A. Safiabadi Tali, J. Song, W. Nam and W. Zhou, *Advanced Optical Materials*, 2021, **9**, 2001908.